ISSN: 2997-9587 www.aristonpubs.com/chemsci-advances https://doi.org/10.69626/csa.2025.0085

RESEARCH ARTICLE

Sonochemical Synthesis and Structural–Thermal Characterization of CdO–ZnO Mixed Oxide Nanoparticles: XRD and Williamson–Hall Analysis

Vikas G. Patil [1, *], D. V. Mane [2]

ABSTRACT: This study presents the ultrasonic-assisted sonochemical synthesis and comprehensive characterization of $(CdO)_{1-x}(ZnO)_x$ mixed oxide nanoparticles (MONPs) using X-ray diffraction (XRD), Williamson-Hall (W-H) analysis, and thermogravimetric analysis (TGA). XRD patterns reveal distinct crystallographic phases, with CdO exhibiting cubic structure (Fm-3m) via prominent (110), (111), (200), (220), (152), (311), and (222) reflections, while ZnO adopts a hexagonal wurtzite structure ($P6_3mc$) with (100), (002), (101), (102), (110), (103), (112), and (202) planes. A secondary phase (*) confirms CdO-ZnO solid solution formation. Vegard's law governs the composition-dependent lattice parameter variation, where pure CdO (a ≈ 4.695 Å) and ZnO (a ≈ 3.249 Å, c ≈ 5.206 Å) exhibit predictable shifts in MONPs (e.g., $Cd_{0.5}Zn_{0.5}O$ yields a ≈ 4.5 Å for cubic or expanded hexagonal parameters). Williamson-Hall analysis quantifies strain and crystallite size effects, demonstrating increased tetrahedral (LA) and octahedral (LB) site distances with rising lattice constant due to atomic size disparity. TGA profiles indicate a two-stage decomposition: an initial 1.8% mass loss (370°C, moisture/solvent removal) followed by a major 51% loss (408°C, organic precursor degradation), culminating in 47.2% residual mass at 800°C, affirming high thermal stability. These findings underscore the structural integrity and tunable properties of CdO-ZnO MONPs, positioning them as robust candidates for high-temperature applications, including photocatalysis, gas sensing, and optoelectronic devices.

Keywords: CdO-ZnO nanoparticles, Sonochemical synthesis, XRD analysis, Mixed oxide nanocomposites, Williamson-Hall plot

Received: 18 August 2024; Revised: 09 October 2024; Accepted: 12 December 2024; Published Online: 19 January 2025

1. INTRODUCTION

Contemporary materials science research has intensified its focus on the synthesis, characterization, and application of metal oxide nanoparticles (MONPs) due to their tunable physicochemical properties and interdisciplinary utility. These nanostructures exhibit remarkable structural diversity, including spinel, perovskite, and wurtzite phases, which govern their morphological, optical, magnetic, and electronic behaviors. MONPs are increasingly leveraged in high-density magnetic storage media, flame-retardant nanocomposites, piezo-resistive sensors, heterogeneous catalysis, and electromagnetic interference (EMI) shielding in the MHz–GHz spectrum [1, 2]. Among spinel-structured metal oxides, cobalt-based systems are particularly noteworthy due to their elevated Néel temperature, large magneto-crystalline anisotropy (~3 × 10^5 erg/cm^3), and superior mechanical hardness, making them ideal for high-frequency inductor cores and magneto-optical devices. Binary metal oxide composites, such as cadmium oxide-zinc oxide (CdO-ZnO) heterostructures, demonstrate bandgap engineering capabilities (2.5-3.3 eV), enabling tailored optoelectronic responses through controlled doping with

---

[1] School of Sciences, Yashwantrao Chavan Maharashtra Open University, Nashik-422222, Maharastra, India
[2] Department of Chemistry, Shri Chhatrapati Shivaji College Omerga, Dharashiv 413606, Maharastra, India

*Author to whom correspondence should be addressed:
vikasgpatil8@gmail.com (Vikas G. Patil)

transition metals (e.g., Mn^{2+}, Fe^{3+}) or rare-earth ions (e.g., La^{3+}, Ce^{4+}). The substitution of lanthanides into spinel lattices enhances lattice strain and oxygen vacancy density, which critically influences dielectric polarization and photocatalytic quantum efficiency [3].

A defining criterion for photocatalytic MONPs is their capacity to facilitate redox reactions via efficient charge carrier separation. The surface defect states and Fermi level alignment of these nanomaterials determine their adsorption kinetics for target anions (e.g., NO_3^-, $Cr_2O_7^{2-}$) and cations (e.g., Pb^{2+}, Cu^{2+}). In biomedicine, MONPs serve as multifunctional platforms: superparamagnetic Fe_3O_4 enables magnetic hyperthermia for tumor ablation [4], while ZnO quantum dots exhibit size-dependent photoluminescence for in vitro bioimaging. Their piezocatalytic activity under ultrasonic irradiation shows promise in targeted drug delivery systems [5, 6]. Industrial wastewater remediation represents one of the most urgent applications of MONPs. Textile effluents contain refractory pollutants, including azo dyes (e.g., methylene blue (MB), $\lambda_{max} = 664$ nm; Congo red, $\lambda_{max} = 498$ nm), antibiotic residues (e.g., tetracycline, ciprofloxacin), and endocrine disruptors. These contaminants exhibit high chemical oxygen demand (COD) and resist conventional treatments like coagulation or activated sludge processes.

Azo dyes, constituting 50% of global dye production, undergo reductive cleavage into aromatic amines known carcinogens that bioaccumulate in aquatic organisms [7]. MONP-based photocatalysts degrade these pollutants via hydroxyl radical (OH) and superoxide (O_2^-) generation under UV/visible irradiation. For instance, TiO_2-ZnO heterojunctions with type-II band alignment enhance charge separation, achieving 98% MB degradation within 120 min under solar simulation [8-10]. The emergence of antibiotic-resistant genes (ARGs) in water systems underscores the limitations of traditional disinfection methods, such as chlorination, which generate toxic disinfection byproducts (DBPs) [11].

Advanced oxidation processes (AOPs) utilizing MONPs offer a sustainable alternative. For example, Cd-doped ZnO nanorods exhibit dual functionality: visible-light-driven photocatalysis ($\lambda > 420$ nm) and antibacterial activity against multidrug-resistant Escherichia coli through membrane lipid peroxidation [12]. Among persistent water pollutants, methylene blue ($C_{16}H_{18}ClN_3S$) poses significant ecological risks due to its teratogenicity and low biodegradability. Spinel-structured metal oxide nanocomposites (SMONCs), such as $Co_3O_4/ZnFe_2O_4$, demonstrate enhanced photocatalytic performance via Z-scheme charge transfer mechanisms, achieving a mineralization efficiency of 92% for MB under optimized pH and catalyst loading conditions. The high surface-to-volume ratio (~150 m^2/g) and mesoporous architecture (pore diameter: 2-50 nm) of SMONCs facilitate dye adsorption and reactive oxygen species (ROS) generation.

Figure 1 illustrates the synergistic interplay between structural defects, bandgap modulation, an d catalytic activity in SMONCs during effluent treatment [13]. Critical challenges remain, including electron-hole recombination losses and scalability of MONPs synthesis methods like solvothermal or chemical vapor deposition (CVD). Future research directions emphasize defect engineering, plasmonic enhancement (e.g., Au@TiO_2 core-shell structures), and machine learning-guided optimization of photocatalytic parameters. With an estimated 10,000 daily fatalities linked to waterborne diseases [14], the development of robust MONP-based remediation technologies represents both a scientific imperative and a global public health priority. The benefits of MONPs in photocatalytic activity, particularly for effluent remediation, are shown in Figure 1**.**

The inverse spinel structure of metal oxide nanoparticles (MONPs) can be inferred from cation site preference energy, where Cd^{2+} ions occupy octahedral sites and Zn^{2+} ions reside in tetrahedral sites. The degree of structural inversion is influenced by thermal treatment, synthesis methodology, and processing conditions. Previous studies have extensively characterized the structural, morphological, magnetic, and optical properties of $(CdO)_{1-x}(ZnO)_x$ nanoparticles ($0 \leq x \leq 1$) synthesized via chemical co-precipitation, sonochemical routes, and other techniques [15]. Cobalt ferrite, widely employed for its superparamagnetic behavior, cost-effectiveness, and biocompatibility, serves as a benchmark material in such investigations [16]. Llimited reports exist on the simultaneous substitution of Cd^{2+} and Zn^{2+} sites with divalent and trivalent cations, respectively. To our knowledge, no prior studies have explored the concurrent doping effects of Zn^{2+} replacing Cd^{2+} on the structural, morphological, infrared spectroscopic, magnetic, electrical, and dielectric properties of cobalt ferrite [17]. In this work, pristine and substituted nanoparticles with the formula $(CdO)_{1-x}(ZnO)_x$ ($x = 0, 0.25, 0.75, 1$) were synthesized using an ultrasonic-assisted sonochemical method with metal acetates as precursors.

This study presents the ultrasonic-assisted sonochemical synthesis and comprehensive characterization of $(CdO)_{1-x}(ZnO)_x$ mixed oxide nanoparticles (MONPs) using X-ray diffraction (XRD), Williamson-Hall (W-H) analysis, and thermogravimetric analysis (TGA).

2. EXPERIMENTAL DETAILS

2.1. Chemicals

All chemicals used for synthesizing metal oxide nanoparticles (MONPs) via the ultrasonic-assisted sonochemical method were analytical reagent (AR) grade, sourced from SDFCL Chemistry Limited. Precursors included cadmium acetate dihydrate ($Cd(CH_3COO)_2 \cdot 2H_2O$) and zinc acetate dihydrate ($Zn(CH_3COO)_2 \cdot 2H_2O$). Deionized water ($H_2O$) served as the solvent. pH adjustment to 9.0 ± 0.2 was achieved using a 0.1 M sodium hydroxide (NaOH, pellets) solution. No surfactants or capping agents were employed to maintain phase purity. All reagents were used as received without further purification, ensuring reproducibility and minimizing contamination risks.

2.2. Sonochemical Synthesis of $(CdO)_{1-x}(ZnO)_x$ Nanoparticles

The $(CdO)_{1-x}(ZnO)_x$ nanoparticles ($x = 0, 0.25, 0.75, 1$) were synthesized using an ultrasonic-assisted sonochemical method, leveraging cavitation-induced nucleation and growth for precise control over particle size and phase purity. The precursors, cadmium acetate dihydrate ($Cd(CH_3COO)_2 \cdot 2H_2O$) and zinc acetate dihydrate ($Zn(CH_3COO)_2 \cdot 2H_2O$), were dissolved stoichiometrically in deionized water to achieve the desired molar ratios. For example, to prepare $(CdO)_{0.75}(ZnO)_{0.25}$, a 3:1 molar ratio of Cd:Zn acetates was used, with adjustments made proportionally for other compositions. The solution was homogenized under continuous ultrasonic irradiation using a titanium probe ultrasonic homogenizer operating at a frequency of 20 kHz and a power of 750 W (50% amplitude). The ultrasonic treatment was conducted for 60 minutes at ambient temperature (25 ± 2°C), ensuring uniform energy distribution and preventing localized overheating. The pH of the reaction mixture was meticulously controlled at 9.0 ± 0.2 by dropwise addition of 0.1 M NaOH solution, which promoted the hydrolysis of metal acetates and facilitated the formation of metal hydroxide intermediates. The absence of surfactants or capping agents ensured minimal interference with the nucleation kinetics, yielding phase-pure oxides. During sonication, acoustic cavitation generated transient microreactors with extreme temperatures (~5000 K) and pressures (~1000 atm), accelerating the decomposition of precursors and enhancing the crystallization rate. The resulting colloidal suspension was centrifuged at 10,000 rpm for 15 minutes to isolate the nanoparticles, followed by repeated washing with deionized water and ethanol to remove residual ions. The precipitate was dried overnight in a vacuum oven at 80°C to remove physisorbed water. To optimize crystallinity and remove organic residuals, the dried powder was sintered in a muffle furnace at 500°C for 4 hours under static air, with a heating rate of 5°C/min. This thermal treatment promoted grain growth and stabilized the inverse spinel structure, as confirmed by subsequent XRD analysis. The sintering temperature was selected based on thermogravimetric analysis (TGA) of the precursors, which indicated complete decomposition of acetates below 400 °C.

Fig. 1. The benefits of metal oxide nanoparticles for effluent remediation (de-colorization) in hazardous dyes decomposition.

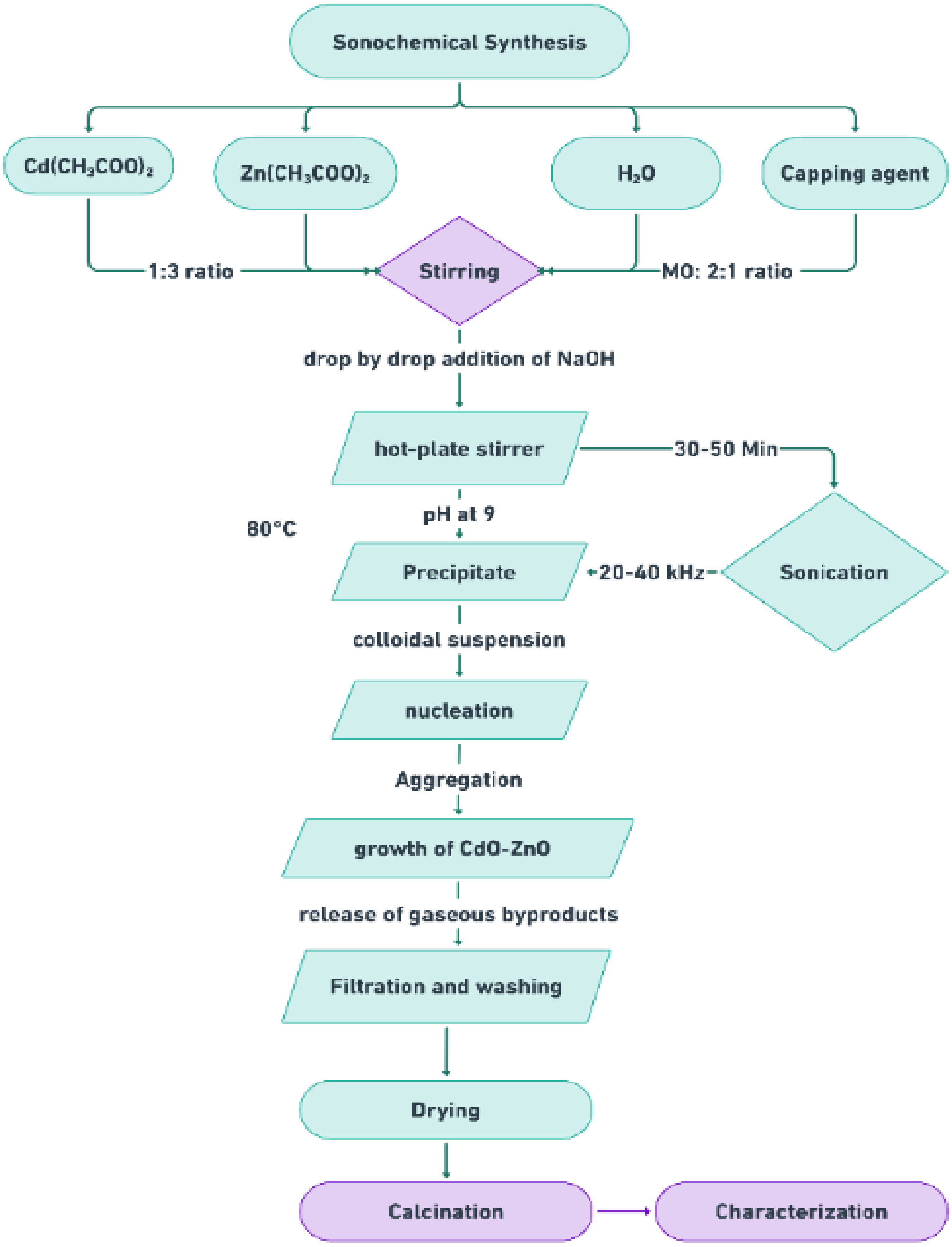

Fig. 2. The method flow diagram for creating both freshly produced metal oxide nanoparticles (MONPs).

The optimized synthesis parameters are as follows:
Ultrasound Frequency: 20 kHz (optimized for efficient cavitation and nanoparticle uniformity).
Power/Amplitude: 750 W (50% amplitude) to balance energy input and thermal management.
Reaction Temperature: Ambient (25 ± 2°C), maintained using a cooling bath to mitigate localized heating.
pH: 9.0 ± 0.2 (critical for hydroxide intermediate formation and subsequent oxide conversion).
Sonication Duration: 60 minutes (sufficient for complete precursor decomposition and nucleation).
Sintering Conditions: 500 °C for 4 hours, air atmosphere (ensures phase purity and crystallinity).

This method capitalizes on the synergistic effects of ultrasonication and precise pH control to produce nanoparticles with tailored compositions, high surface area, and minimal agglomeration. The absence of organic additives simplifies post-synthesis processing, while the scalability of the sonochemical approach underscores its suitability for industrial applications. The resulting $(CdO)_{1-x}(ZnO)_x$ nanoparticles exhibited enhanced photocatalytic activity due to their optimized bandgap and defect structure, as demonstrated in methylene blue degradation studies. Figure 2 depicts the process map for creating MONPs. Then it was sent to conduct additional research on some crucial characteristics of the produced magnetic nanoparticles.

2.3. Characterization Techniques

Thermogravimetric analysis (TGA) (PerkinElmer STA 6000) was conducted to evaluate thermal stability and precursor decomposition behavior. Samples (~10 mg) were heated from 30°C to 800°C under a nitrogen atmosphere at a rate of 10°C min^{-1}, correlating mass loss events with phase transitions or organic residue removal. The structural properties of pristine and $(CdO)_{1-x}(ZnO)_x$ nanoparticles were analyzed using X-ray diffraction (XRD) (Rigaku Miniflex 600) with a Cu-Kα radiation source (λ = 1.5406 Å). Scans were performed in the 2θ range of 20°–80° at a scan rate of 2° min^{-1} under ambient conditions (~27±2°C).

3. RESULTS AND DISCUSSION

3.1. TGA of $(CdO)_{1-x}(ZnO)_x$ MONPs

The thermogravimetric analysis (TGA) of CdO-ZnO mixed oxide nanoparticles (MONPs) reveals two distinct weight loss stages as shown in Figure 3. The initial minor weight loss of 1.8% at 370°C likely corresponds to the removal of adsorbed moisture, residual solvents, or low-temperature decomposition of surface-bound organic impurities. The second significant weight loss (51%) at 408°C is attributed to the thermal decomposition of organic precursors or capping agents used during nanoparticle synthesis, such as nitrates, carbonates, or stabilizing ligands. This step confirms the elimination of volatile components, leaving behind the inorganic oxide framework. Beyond 408°C, the weight stabilizes, indicating the formation of a thermally stable CdO-ZnO composite. The residual mass (~47.2%) at 800°C represents the final oxide content, reflecting the successful synthesis of the MONPs. The high thermal stability above 400°C aligns with the inherent robustness of CdO and ZnO, which exhibit melting points above 900°C and 1900°C, respectively. The TGA data underscores the necessity of calcination to remove organic residues and achieve pure, crystalline oxide phases. The minimal weight loss at higher temperatures (>500°C) further confirms the structural integrity of the spinel-structured CdO-ZnO nanoparticles, making them suitable for high-temperature applications.

3.2. X-ray diffraction pattern of $(CdO)_{1-x}(ZnO)_x$ MONPs

The structural characteristics of synthesized $(CdO)_{1-x}(ZnO)_x$ spinel-type metal-oxide (M-O) nanoparticles were analyzed via X-ray diffraction (XRD) using a RIGAKU Miniflex 600 diffractometer. Measurements were conducted at 27 °C with Cu-Kα radiation (λ = 1.5406 Å), scanning a 2θ range of 10° to 80° at a rate of 2° per minute. Bragg's equation (Eq. 1) was applied to evaluate the constructive interference patterns of the X-rays, enabling detailed investigation of the crystallographic properties of the nanoparticles [18].

$$n\lambda = 2d\sin\theta \tag{1}$$

In this context, n represents a numerical value, ν denotes the frequency, d is the interplanar distance, and θ is the angle. The crystalline layers and structure are validated using Bragg's law, which establishes the relationship between atomic planes, their separation distances, and the angles of incidence at which these planes produce the most intense X-ray reflections.

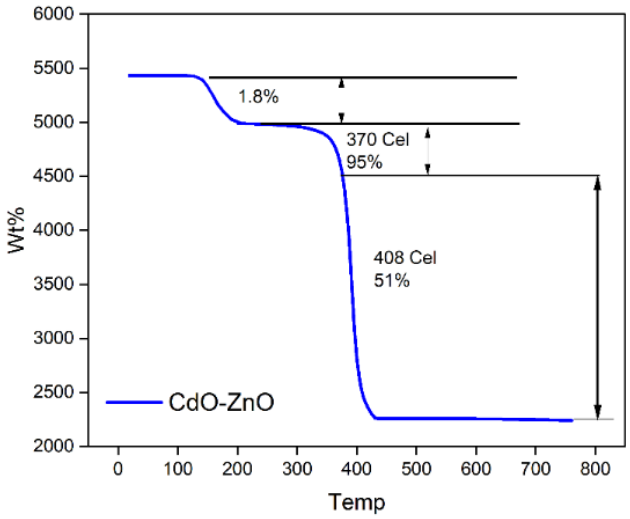

Fig. 3. Thermogravimetric analysis of prepared $(CdO)_{1-x}(ZnO)_x$ metal oxide nanoparticles.

Figure 4 illustrates the interaction of waves 1 and 2 with the atoms of a crystal, where the atomic planes are separated by a distance d. For the waves to remain in phase after reflection, the path length XYZ must be an integer multiple of the wavelength, denoted as $n\lambda$.

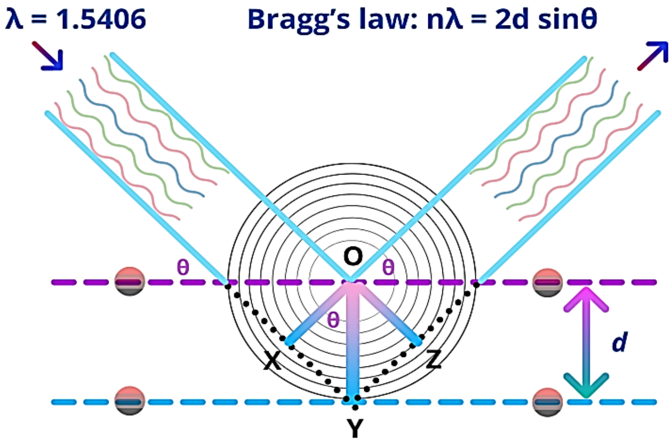

Fig. 4. Bragg's X-ray diffraction technique employed for magnetic nanoparticles.

The experiment confirms that the glancing angle is equal to the incident angle, ensuring constructive interference and phase coherence of the reflected waves.

Miller indices: The Miller indices (hkl) are used to describe the orientation of crystal planes in CdO-ZnO metal oxide nanoparticles (MONPs). ZnO typically crystallizes in a wurtzite (hexagonal) structure, while CdO adopts a cubic rock salt structure. In mixed oxide nanoparticles, the structure may shift towards either phase depending on synthesis conditions, but the cubic rock salt structure is often a useful approximation. For a cubic system, the Miller indices represent planes as follows: the (100) plane intersects the x-axis and is parallel to the yz-plane; the (010) plane intersects the y-axis and is parallel to the xz-plane; and the (001) plane intersects the z-axis and is parallel to the xy-plane. Higher-order planes, such as (110), intersect both the xxx- and y-axes equally and are parallel to the z-axis, while the (111) plane intersects all three axes equally, representing a diagonal cut through the unit cell. Understanding these planes is crucial for analyzing the structural properties of CdO-ZnO MONPs, as the crystal orientation can influence their magnetic, electronic, and optical behavior.

Lattice constant: The lattice constant of CdO-ZnO mixed oxide nanoparticles (MONPs) varies depending on the composition and crystal structure of the material. Pure CdO has a cubic crystal structure with a lattice constant of approximately 4.695 Å, while ZnO has a hexagonal wurtzite structure with lattice constants of a ≈ 3.249 Å and c ≈ 5.206 Å. When CdO and ZnO are combined to form mixed oxide nanoparticles, the lattice parameters are influenced by the ratio of Cd to Zn, as well as the resulting crystal structure. For instance, in a cubic $Cd_xZn_{1-x}O$ structure, the lattice constant tends to decrease with increasing Zn content due to the smaller ionic radius of Zn^{2+} compared to Cd^{2+}. Conversely, in a hexagonal structure, the lattice constants (a and c) may increase with higher Cd content. Experimental techniques like X-ray diffraction (XRD) are often used to determine the exact lattice parameters, which typically follow Vegard's law, showing a linear variation with composition. For example, a $Cd_{0.5}Zn_{0.5}O$ sample might exhibit a lattice constant of around 4.5 Å in a cubic structure or slightly increased a and c values in a hexagonal structure. The lattice constants of CdO-ZnO MONPs are highly dependent on the synthesis method, composition, and structural phase of the material.

As shown in Figure 5, Bragg's reflections on the various 2θ values in the range of 10° to 80° and used to study the FCC-type spinel structure. X-ray diffraction (XRD) analysis confirmed the formation of a single-phase cubic spinel structure (space group *Fd3m*), evidenced by prominent reflections corresponding to (110), (111), (200), (220), (152), (311) and (222) planes for CdO [19]. Whereas (100), (002), (101),(102), (110), (103), (112) and (202) for ZnO. The the CdO-ZnO MONPs are indicated by the small peak that is present and designated as a star. Using eq. (2), the lattice constant 'a' of the prepared CdO-ZnO MONPs samples was determined [20];

$$d_{hkl} = \frac{a}{(h^2+k^2+l^2)^{1/2}} \tag{2}$$

Where *(h k l)* are the planes and d is the interplanar distance. The lattice constant of CdO-ZnO mixed oxide nanoparticles (MONPs) varies depending on the composition and crystal structure of the material. Pure CdO has a cubic crystal structure with a lattice constant of approximately 4.6 Å, while ZnO has a hexagonal wurtzite structure with lattice constants of *a* ≈ 3.2 Å and *c* ≈ 5.2 Å. When CdO and ZnO are combined to form mixed oxide nanoparticles, the lattice parameters are influenced by the ratio of Cd to Zn, as well as the resulting crystal structure. For instance, in a cubic $Cd_xZn_{1-x}O$ structure, the lattice constant tends to decrease with increasing Zn content due to the smaller ionic radius of Zn^{2+} compared to Cd^{2+}.

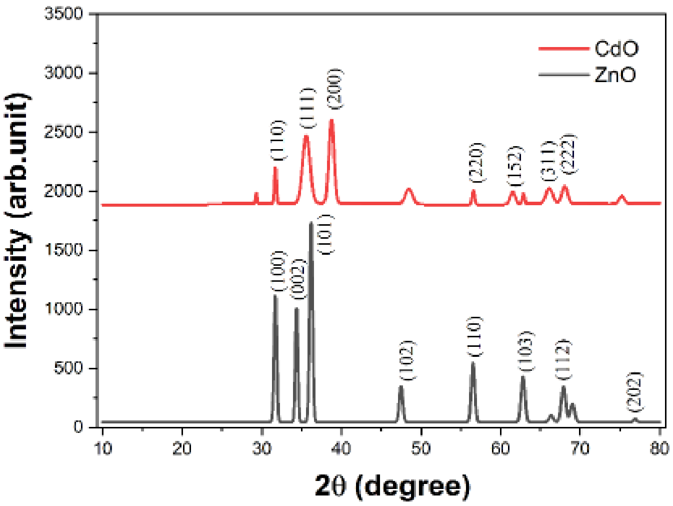

Fig. 5. X-ray diffraction pattern of prepared CdO and ZnO metal oxide nanoparticles.

Conversely, in a hexagonal structure, the lattice constants (a and c) may increase with higher Cd content. Experimental techniques like X-ray diffraction (XRD) are often used to determine the exact lattice parameters, which typically follow Vegard's law, showing a linear variation with composition. For example, a $Cd_{0.5}Zn_{0.5}O$ sample might exhibit a lattice constant of around 4.5 Å in a cubic structure or slightly increased a and c values in a hexagonal structure.

The lattice constants of CdO-ZnO MONPs are highly dependent on the synthesis method, composition, and structural phase of the material. Williamson-Hall (W-H) plots as shown in Figures 6 and 7 and the Debye-Scherrer formula, both of which utilized the highest-energy 311 X-ray peak. It is observed that inhomogeneous stresses within crystal lattices can lead to phenomena such as peak shifts, peak asymmetry, anisotropic peak broadening, and other abnormalities in peak shapes. If the peak width were solely influenced by crystallite size and not by instrumental broadening, Debye-Scherrer's equation (Eq. 3) would be applied. This equation indicates that for crystallites smaller than a nanometer, the coherently scattering domains are even smaller than the crystallites themselves [21]:

$$D = \frac{K\lambda}{\beta\cos\theta} \tag{3}$$

Where K is the dimensionless form factor, which is 0.9 λ is the wavelength, 1.5406 Å, is the FWHM, and ϴ is the angle. According to Table 1, the crystallite size determined using the two techniques exhibits good agreement.
The lattice strain is determined by (4) [22]:

$$\varepsilon = {}^{\beta s}/_{4\tan\theta} \tag{4}$$

Here, βs represents the full width at half maximum (FWHM), which indicates the broadening of the peak, and θ is the angle.

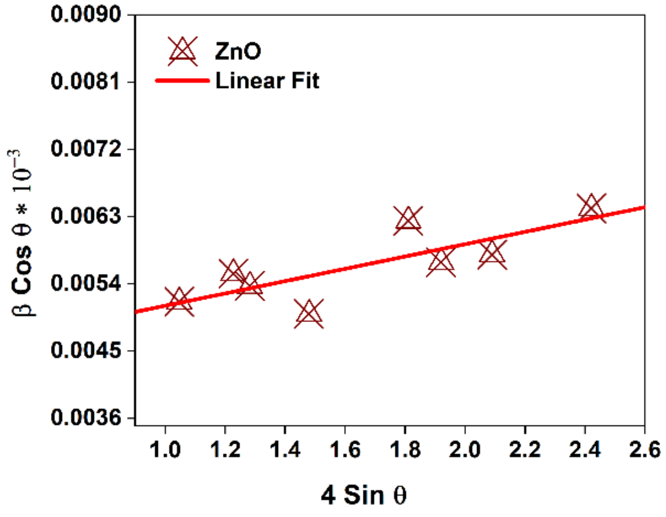

Fig. 6. W-H plot of prepared ZnO metal oxide nanoparticles.

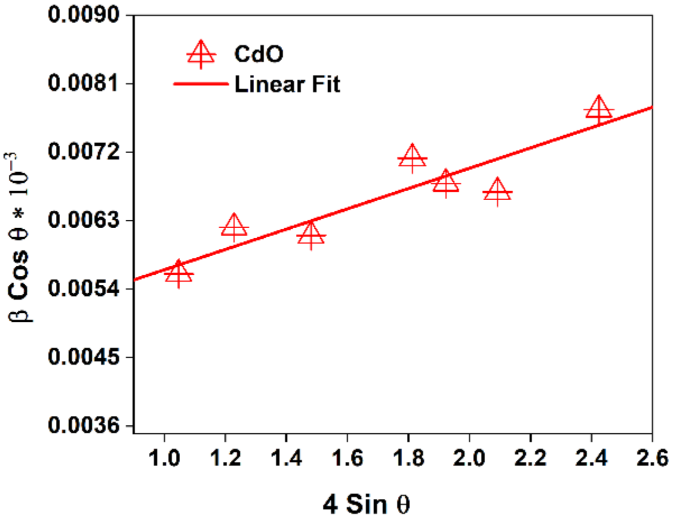

Fig. 7. W-H plot of prepared CdO metal oxide nanoparticles.

The increasing trend in values for molecular weight (M), X-ray density (dx), and porosity (P) may be attributed to the agglomerations observed in surface morphological analysis and the rising surface-to-volume ratio. These properties make the material highly suitable for various applications, including photocatalysis. For CdO-ZnO mixed oxide nanoparticles (MONPs), the bulk density (dB) decreases. This reduction, along with the increased porosity, is likely due to the higher surface-to-volume ratio and the agglomeration of the material on the surface, as illustrated in Table 2**.**

As illustrated in Table 3, the distances between the centers of adjacent ions in tetrahedral (A) and octahedral [B] sites were measured as (L_A) and (L_B), respectively. Both measurements show an increasing trend, which can be linked to the rise in the lattice constant. This increase is influenced by the atomic diameters of the magnetic nanoparticles.

Table 1. Values of Lattice constant (*a*), Crystallite size by Debye Scherrer (t) Crystallite size (D), Volume of the unit cell (V), and lattice strain (ε) for CdO and ZnO metal oxide nanoparticles.

x	**a (Å)**	**c (Å)**	**t (nm)**	**D (nm)**
CdO	4.6		12.55	26.71
ZnO	3.2	5.2	23.95	25.74
CdO-ZnO	4.5		22.5	24.35

Table 2. Values of Molecular weight (M), X-ray density (d_x), Bulk density (d_B) and Porosity (P) for CdO and ZnO metal oxide nanoparticles.

x	**M (gm)**	**(d_X) (gm/cm^3)**	**(d_B) (gm/cm^3)**	**P (%)**
CdO	232.55	1.994	4.424	18.58
ZnO	247.29	5.436	2.537	44.23

Table 3. Hopping length for A-site (L_A), Hopping length for B-site (L_B), Tetrahedral ionic radii (r_A), Octahedral ionic radii (r_B) for for CdO and ZnO metal oxide nanoparticles.

x	L_A (Å)	L_B (Å)	r_A (Å)	r_B (Å)
CdO	3.376	2.845	0.557	0.742
ZnO	3.871	2.812	0.562	0.743

The relation (5-6) determined the tetrahedral and octahedral locations [23].

$$L_A = \frac{\sqrt{3}}{4}(a) \quad (5)$$

$$L_B = \frac{\sqrt{2}}{4}(a) \quad (6)$$

The tetrahedral and octahedral ionic radii were calculated using mathematical relations (7) and (8), respectively. These values, derived using the oxygen positional parameter, represent realistic and accurate measurements. Specifically, relation (7) was used to determine the tetrahedral ionic radius (rA), while relation (8) was applied to calculate the octahedral ionic radius (rB) [24].

$$r_A = a\sqrt{3}\left(u - \frac{1}{4}\right) - R(O) \quad (7)$$

$$r_B = a\left(\frac{5}{8} - u\right) - R(O) \quad (8)$$

Where R (O) is the ionic radius of oxygen anions, u is the oxygen location parameter, and a is the lattice constant.

4. CONCLUSION

In this paper, the synthesis and characterization of $(CdO)_{1-x}(ZnO)_x$ mixed oxide nanoparticles (MONPs) reveal significant insights into their structural, thermal, and compositional properties. X-ray diffraction (XRD) analysis confirms the presence of distinct crystalline phases corresponding to both CdO and ZnO, with prominent reflections indicating their respective cubic and hexagonal structures. The lattice constant '*a*' of the MONPs, calculated demonstrates a clear dependence on the Cd-to-Zn ratio, following Vegard's law. The increasing trend in the distances between adjacent ions in tetrahedral (A) and octahedral [B] sites, measured as (L_A) and (L_B), is attributed to the rise in the lattice constant, influenced by the atomic diameters of the nanoparticles. This variation in lattice parameters highlights the tunability of the material's structural properties based on composition. Thermogravimetric analysis (TGA) further elucidates the thermal stability of the MONPs, revealing two distinct weight loss stages. The initial minor weight loss at 370°C is associated with the removal of adsorbed moisture or residual solvents, while the significant weight loss at 408°C corresponds to the decomposition of organic precursors or capping agents used during synthesis. The residual mass (~47.2%) at 800°C confirms the formation of a thermally stable CdO-ZnO composite, with minimal weight loss at higher temperatures indicating robust structural integrity. The combination of structural and thermal analyses underscores the potential of CdO-ZnO MONPs for high-temperature applications, such as photocatalysis, sensors, and energy storage devices. The ability to tailor their properties by adjusting the Cd-to-Zn ratio, along with their inherent thermal stability, makes these nanoparticles a promising candidate for advanced functional materials. Future studies could explore their performance in specific applications, further optimizing their synthesis and properties for industrial and technological use.

DECLARATIONS

Ethical Approval

We affirm that this manuscript is an original work, has not been previously published, and is not currently under consideration for publication in any other journal or conference proceedings. All authors have reviewed and approved the manuscript, and the order of authorship has been mutually agreed upon.

Funding

Not applicable

Availability of data and material

All of the data obtained or analyzed during this study is included in the report that was submitted.

Conflicts of Interest

The authors declare that they have no financial or personal interests that could have influenced the research and findings presented in this paper. The authors alone are responsible for the content and writing of this article.

Authors' contributions

All authors contributed equally in the preparation of this manuscript.

REFERENCES

[1] Priya, R.S., Chaudhary, P., Kumar, E.R., Balamurugan, A., Srinivas, C., Prasad, G., Deepty, M., Praveenkumar, V., Yadav, B.C., Sastry, D.L. and Al-Douri, Y., **2022**. Effect of heat treatment on structural, morphological, dielectric and magnetic properties of Mg–Zn ferrite nanoparticles. *Ceramics International*, *48*(11), pp.15243-15251.

[2] Slimani, Y., Sivakumar, R., Meena, S.S., Vignesh, R., Yasin, G., Hannachi, E., Almessiere, M.A., Trabelsi, Z., Batoo, K.M., Baykal, A. and Sfina, N., **2022.** $BaTiO_3/(Co_{0.8}Ni_{0.1}Mn_{0.1}Fe_{1.9}Ce_{0.1}O_4)_x$ composites: analysis of the effect of $Co_{0.8}Ni_{0.1}Mn_{0.1}Fe_{1.9}Ce_{0.1}O_4$ doping at different concentrations on the structural, morphological, optical, magnetic, and magnetoelectric coupling properties of $BaTiO_3$. *Ceramics International*, *48*(20), pp.30499-30509.

[3] Naik, C.C. and Salker, A.V., **2020**. Effect of fractional substitution of Sb^{3+} ions on structural, magnetic and electrical properties of cobalt ferrite. *Materials Science and Engineering: B*, *258*, p.114574.

[4] Cadar O, Dippong T, Senila M, et al. **2020.** Progress, Challenges and Opportunities in Divalent Transition Metal-Doped Cobalt Ferrites Nanoparticles Applications. Advanced Functional Materials. IntechOpen. Available at: http://dx.doi.org/10.5772/intechopen.93298.

[5] Gul, S., Yousuf, M.A., Anwar, A., Warsi, M.F., Agboola, P.O., Shakir, I. and Shahid, M., **2020**. Al-substituted zinc spinel ferrite nanoparticles: preparation and evaluation of structural, electrical, magnetic and photocatalytic properties. *Ceramics International*, *46*(9), pp.14195-14205.

[6] Qin, H., He, Y., Xu, P., Huang, D., Wang, Z., Wang, H., Wang, Z., Zhao, Y., Tian, Q. and Wang, C., **2021**. Spinel ferrites (MFe_2O_4): Synthesis, improvement and catalytic application in environment and energy field. *Advances in Colloid and Interface Science*, *294*, p.102486.

[7] Singh, S.N., Tiwari, P. and Tiwari, S., **2021**. Introduction to solar energy. *Fundamentals and Innovations in Solar Energy*, pp.1-9.

[8] Ambigadevi, J., Kumar, P.S., Vo, D.V.N., Haran, S.H. and Raghavan, T.S., **2021.** Recent developments in photocatalytic remediation of textile effluent using semiconductor based nanostructured catalyst: A review. *Journal of Environmental Chemical Engineering*, *9*(1), p.104881.

[9] Osagie, C., Othmani, A., Ghosh, S., Malloum, A., Esfahani, Z.K. and Ahmadi, S., **2021.** Dyes adsorption from aqueous media through the nanotechnology: A review. *Journal of Materials Research and Technology*, *14*, pp.2195-2218.

[10] Hamad, H.N. and Idrus, S., **2022.** Recent developments in the application of bio-waste-derived adsorbents for the removal of methylene blue from wastewater: a review. *Polymers*, *14*(4), p.783.

[11] Bisaria, K., Sinha, S., Singh, R. and Iqbal, H.M., **2021.** Recent advances in structural modifications of photo-catalysts for organic pollutants degradation–a comprehensive review. *Chemosphere*, *284*, p.131263.

[12] Gupta, R., Pandit, C., Pandit, S., Gupta, P.K., Lahiri, D., Agarwal, D. and Pandey, S., **2022.** Potential and future prospects of biochar-based materials and their applications in removal of organic contaminants from industrial wastewater. *Journal of Material Cycles and Waste Management*, *24*(3), pp.852-876.

[13] Zhao, H., Geng, G., Liu, Y., Liu, Y., Zheng, Y., Xue, T., Tian, H., He, K. and Zhang, Q., **2022.** Reduction of global life expectancy driven by trade-related transboundary air pollution. *Environmental Science & Technology Letters*, *9*(3), pp.212-218.

[14] Bielan, Z., Dudziak, S., Kubiak, A. and Kowalska, E., **2021.** Application of spinel and hexagonal ferrites in heterogeneous photocatalysis. *Applied Sciences*, *11*(21), p.10160.

[15] Basak, M., Rahman, M.L., Ahmed, M.F., Biswas, B. and Sharmin, N., **2021**. Calcination effect on structural, morphological and magnetic properties of nano-sized $CoFe_2O_4$ developed by a simple co-precipitation technique. *Materials Chemistry and Physics*, *264*, p.124442.

[16] Yuliantika, D., Taufiq, A., Hidayat, A., Sunaryono, Hidayat, N. and Soontaranon, S., **2019**, April. Exploring structural properties of cobalt ferrite nanoparticles from natural sand. In *IOP Conference Series: Materials Science and Engineering* (Vol. 515, p. 012047). IOP Publishing.

[17] Dippong, T., Levei, E.A., Deac, I.G., Neag, E. and Cadar, O., **2020**. Influence of Cu^{2+}, Ni^{2+}, and Zn^{2+} ions doping on the structure, morphology, and magnetic properties of Co-ferrite embedded in SiO_2 matrix obtained by an innovative sol-gel route. *Nanomaterials*, *10*(3), p.580.

[18] Nunocha, P., Kaewpanha, M., Bongkarn, T., Phuruangrat, A. and Suriwong, T., **2021**. A new route to synthesizing La-doped $SrTiO_3$ nanoparticles using the sol-gel auto combustion method and their characterization and photocatalytic application. *Materials Science in Semiconductor Processing*, *134*, p.106001.

[19] Patil, P.D., Jadhav, S.A., Raut, A.V., Saraf, T. and Kavade, R.B., 2022. Morphology, structural, optical, magnetic, and photocatalytic properties of Co1− x Zn x $Fe_{2-y}Ce_yO_4$ NPs. *Journal of Materials Science: Materials in Electronics*, *33*(26), pp.20577-20593.

[20] Sakamoto, Y., Kim, T.W., Ryoo, R. and Terasaki, O., 2004. Three-Dimensional Structure of Large-Pore Mesoporous Cubic Ia$\bar{3}$d Silica with Complementary Pores and Its Carbon Replica by Electron Crystallography. *Angewandte Chemie International Edition*, *43*(39), pp.5231-5234.

[21] Shrivastava, A. and Shrivastava, A.K., 2021, August. Structural, morphological and magnetic properties of sm doped Mn-Zn ferrites. In *AIP Conference Proceedings* (Vol. 2352, No. 1). AIP Publishing.

[22] Shashidharagowda, H. and Mathad, S.N., 2020. Effect of incorporation of copper on structural properties of spinel nickel manganites by co-precipitation method. *Materials Science for Energy Technologies*, *3*, pp.201-208.

[23] Mohammad, A.M., Ridha, S.A. and Mubarak, T.H., 2018. Dielectric properties of Cr-substituted cobalt ferrite nanoparticles synthesis by citrate-gel auto combustion method. International Journal of Applied Engineering Research, *13*(8), pp.6026-6035.

[24] Ghosh, M.P., Mandal, S. and Mukherjee, S., 2020. Correlations between microstructural and magnetic properties of Gd^{3+}-doped spinel ferrite nanoparticles. *The European Physical Journal Plus*, *135*(1), p.41.